ACS APPLIED MATERIALS & INTERFACES
Research Article
www.acsami.org

Platinum-Enhanced Electron Transfer and Surface Passivation through Ultrathin Film Aluminum Oxide (Al_2O_3) on Si(111)−CH_3 Photoelectrodes

Hark Jin Kim, Kara L. Kearney, Luc H. Le, Ryan T. Pekarek, and Michael J. Rose*

Department of Chemistry, The University of Texas at Austin, Austin, Texas 78712, United States

Supporting Information

ABSTRACT: We report the preparation, stability, and utility of Si(111)−CH_3 photoelectrodes protected with thin films of aluminum oxide (Al_2O_3) prepared by atomic layer deposition (ALD). The photoelectrodes have been characterized by X-ray photoelectron spectroscopy (XPS), photoelectrochemistry (Fc in MeCN, Fc−OH in H_2O), electrochemical impedance spectroscopy (EIS), and cyclic voltammetry (CV) simulation. XPS analysis of the growing Al_2O_3 layer affords both the thickness, and information regarding two-dimensional versus three-dimensional mode of growth. Impedance measurements on Si(111)|CH_3|Al_2O_3 devices reveal that the nascent films (5−30 Å) exhibit significant capacitance, which is attenuated upon surpassing the bulk threshold (∼30 Å). The Al_2O_3 layer provides enhanced photoelectrochemical (PEC) stability evidenced by an increase in the anodic window of operation in MeCN (up to +0.5 V vs Ag) and enhanced stability in aqueous electrolyte (up to +0.2 V vs Ag). XPS analysis before and after PEC confirms the Al_2O_3 layer is persistent and prevents surface corrosion (SiO_x). Sweep-rate dependent CVs in MeCN at varying thicknesses exhibit a trend of increasingly broad features, characteristic of slow electron transport kinetics. Simulations were modeled as slow electron transfer through a partially resistive and electroactive Al_2O_3 layer. Lastly, we find that the Al_2O_3 ultrathin film serves as a support for the ALD deposition of Pt nanoparticles ($d \approx 8$ nm) that enhance electron transfer through the Al_2O_3 layer. Surface recombination velocity (SRV) measurements on the assembled Si(111)|CH_3|Al_2O_3-15 device affords an S value of 4170 cm s^{-1} (τ = 4.2 μs) comparable to the bare Si(111)−CH_3 surface (3950 cm s^{-1}; τ = 4.4 μs). Overall, the results indicate that high electronic quality and low surface defect densities can be retained throughout a multistep assembly of an integrated and passivated semiconductor|thin-film|metal device.

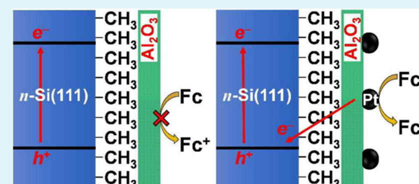

KEYWORDS: *methyl-passivated Si(111), Al_2O_3 passivation, atomic layer deposition, platinum (Pt) ALD, electron transport*

1. INTRODUCTION

The use of earth abundant elements is a crucial part of making solar energy conversion devices available at large scale for low cost,[1−3] and silicon remains a primary focus in this field because of its low material cost and high earth abundance. However, in semiconductor/liquid junction devices, degradation of the silicon surface is the primary factor for loss of device performance over time. For example, silicon photoelectrodes [Si(111), E_g = 1.12 eV, indirect] have been modified with various metallic and metal oxide compositions, affording catalytically active surfaces for water oxidation or reduction;[4,5] however, the surfaces were unstable (typical for Si) with respect to corrosion and ensuing formation of electronically deficient SiO_x species at the surface. Therefore, it is of interest to develop an electronically passivating and chemically protecting layer to preserve device performance. In 1996, Lewis and co-workers reported a two-step procedure for passivating Si(111) surfaces with a monolayer of methyl groups, forming atomically flat and well-defined Si−CH_3 atop sites at ∼100% coverage.[6] This surface exhibited high electronic quality [low surface recombination velocity (SRV)], a high V_{OC} value (n-type with ferrocyanide), and an excellent fill factor.[7] Since that finding, a variety of surface R-groups (ethyl, phenyl, thienyl, allyl, etc.) have been covalently bonded to the surface in electroactive devices.[8,9] However, the organic-only passivation methods on silicon remain largely unsuitable for photocells constructed with aqueous (or residually hydrated organic) electrolytes.[10] The intrusion of H_2O into defect sites even at the 10^{-6} to 10^{-9} surface defect density rapidly forms SiO_x layers that are both insulating and electronically defective.

Another approach to passivating the semiconductor/liquid junction involves the use of a thin layer of transparent, chemically resistant material such as a metal oxide. For example, the electronic effects of atomic layer deposition of aluminum oxide (Al_2O_3) on both Si(100) and Si(111) surfaces have been reported, wherein the Si(111) was proven to be more difficult to passivate.[11−13] Devices of type Si(100)/Al_2O_3 retained reasonable electronic response, but remained sub-optimal compared to freshly HF-etched Si(100).[11−13] The electronic performance metrics of Si(111)|Al_2O_3-oriented devices were severely compromised following alumina deposition, and a complete loss of electronic response was observed.[11]

Received: January 15, 2015
Accepted: April 6, 2015
Published: April 16, 2015

ACS Publications © 2015 American Chemical Society

DOI: 10.1021/acsami.5b00376
ACS Appl. Mater. Interfaces 2015, 7, 8572−8584

Overall, the differential effects between Si(100) and Si(111) were ascribed to the propensity for high defect densities on the unfunctionalized Si(111) surface. Indeed, the singular nature of the atop Si sites on Si(111) surfaces (i.e., one bond up) renders the surface very sensitive to surface defects. The Si(100) surface is inherently nonuniform (one and two bonds up are possible on atop Si), and is thus less prone to changes in the defect density.

Some reports have indicated that Al_2O_3 thin films can provide some extent of surface passivation by both field effect passivation and chemical passivation; both have been proposed to decrease the electron−hole pair recombination rate at the semiconductor−liquid junction.[11,14] In 2011, Kessels et al. reported significant differences of surface recombination velocity (S_{eff}) in ALD Al_2O_3 passivation; H_2O-based thermal ALD showed a higher level of passivation ($S_{eff} < 30$ cm s^{-1}) than plasma ALD ($S_{eff} < 3 \times 10^3$ cm s^{-1}).[15] Relatedly, Ley et al. reported formation of an Si−O−Al bond in the Si|Al_2O_3 interface when ALD was performed on H-terminated Si substrate.[16] Unfortunately, the Si−O−Al bonds result in an atomically rough interlayer between the Al_2O_3 and Si layers, which was accompanied by deficient electronic properties.[17]

One disadvantage of Al_2O_3 for charge-transfer applications is its insulating nature. For example, George et al.'s reports have shown that films as thin as 50 Å effectively block charge-transfer across interfaces.[18] This is not surprising, given the low dielectric constant (∼9) and insulating properties of bulk Al_2O_3. However, recent work has shown that the apparently resistive properties of thin, insulating films can be overcome by the deposition of fixed metal nanoparticles (or other conductive entity) on the insulating layer. For example, Fermín and co-workers assembled devices using insulating PMA/polymer (thickness of ∼2 nm) on Au electrodes, wherein the charge transport is rescued by the application of Au nanoparticles on the polymer surface.[19] Relatedly, Bard and co-workers reported that the charge-transfer properties of a resistive Pt|TiO_2 interface (thickness of ∼2 nm) were rescued by the adsorption of single Pt nanoparticles dispersed in solution.[20] To accompany this, theoretical studies by Chazalviel and Gooding have investigated this effect, and suggest that the higher density of states presented by fixed metal nanoparticles (as compared to a millimolar solution redox agent at the interface) enhances the observed electron transfer rate.[21,22] This phenomenon was attributed to a higher probability of tunneling from the substrate (through the insulating layer) to the destination particle.

On the basis of the above information regarding Si surface passivation and charge-transfer across insulating films, we surmised that an H_2O-based ALD method would provide beneficial passivation results on Si and that the common Si(111)−H substrate was not a suitable candidate for direct ALD deposition due to the certainty of forming electronically poor SiO_x during the deposition. In this work, we report that the use of an organic passivating layer in conjunction with an inorganic thin film provides functional and stable Si(111) photoelectrodes (Scheme 1). The composite devices exhibit high stability under cathodic and mildly anodic conditions in organic and aqueous solvent. Such *n*-type devices of formulation Si(111)|CH_3|Al_2O_3 routinely and reproducibly cycle the Fc−OH/Fc−OH^+ redox couple in aqueous solution under 1 sun illumination, at positive potentials relative to the Ag/Ag^+ reference electrode. A platinized *n*-type device of type *n*-Si(111)|CH_3|Al_2O_3|Pt has been constructed using sequential atomic layer depositions of Al_2O_3 and Pt metal (plasma-free), which was only recently described.[23,24] This resulting semiconductor|insulator|metal (SIM) assembly achieves substantial electron transport at insulator thicknesses up to 40 Å. The device also features excellent stability in repeated anodic CV sweeps (up to +0.5 V in MeCN, +0.2 V in H_2O) and is stable under ambient atmosphere for months without the need to re-etch with HF prior to use.

Scheme 1. Diagram of the Photoelectrode Structure Pursued in This Work

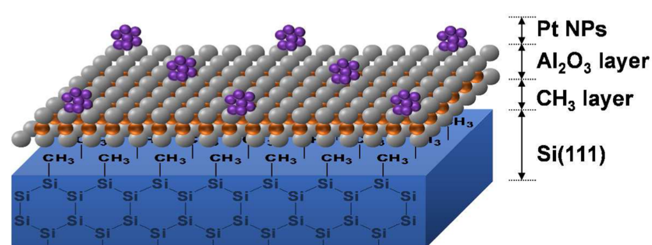

2. EXPERIMENTAL SECTION

2.1. Preparation of Si(111) Photoelectrode. *2.1.1. Preparation of Methyl-Terminated Si(111) Substrate.*[6] Single-side-polished *n*-type Si(111) wafers (phosphorus-doped, Cz grown, thickness 350 ± 25 μm, resistivity 1−10 Ω·cm) were purchased from Virginia Semiconductor. Prior to surface modification, the silicon wafers were diced into 1.0 cm^2 pieces. Wafers were sequentially cleaned by sonication for 10 min with acetone, ethanol, and water and subsequently dried by a stream of N_2 gas. Organic residues were removed by immersing wafers in Piranha solution prepared from 1:3 mixture of hydrogen peroxide (30%, Fisher Scientific) to sulfuric acid (96.6%, Fisher Scientific) at 90 °C for 10 min. After the Piranha wash, wafers were thoroughly rinsed with excess deionized water. Then, wafers were immersed in buffered HF (aq) solution (semiconductor grade, Transene Company, Inc.) for 10 s to remove the oxide layer. After the HF (aq) solution was drained, wafers were thoroughly rinsed with excess deionized water to remove any remaining HF on the surface. The atomically flat Si(111)−H surface was achieved by immersing wafers in a degassed NH_4F solution for 20 min (semiconductor grade, Transene Company, Inc.) using N_2 bubbling. The NH_4F solution had been degassed using N_2 bubbling at least 30 min prior to wafer immersion. During immersion, wafers were agitated periodically to remove bubble formation on the surface. After the NH_4F solution was drained, Si−H wafers were rinsed with water and dried under a stream of N_2 gas. Within 5 min, Si−H wafers were transferred to a glovebox under N_2 atmosphere (to avoid oxidation to SiO_x). Next, the Si−H bond was chlorinated by immersing the wafers in PCl_5 (metal basis, 99.998%, Alfa Aesar) saturated in chlorobenzene (99.8%, Sigma-Aldrich) solution at 90 °C for ∼50 min. One grain of benzoyl peroxide (reagent grade, 97%, Sigma-Aldrich) was added to PCl_5 solution to initiate the reaction. After chlorination, Si−Cl wafers were thoroughly rinsed with chlorobenzene to remove residual PCl_5, followed by THF. Methylation was performed by immersing the Si−Cl wafers in 1 M CH_3MgCl solution prepared from 1:2 dilution of CH_3MgCl (3.0 M in THF, Sigma-Aldrich) in THF at 60 °C for 30 min. After the methylation, Si−CH_3 wafers were thoroughly rinsed with THF and removed from the glovebox. Finally, the Si−CH_3 wafers were sequentially cleaned by sonication for 10 min with acetone, ethanol, and water (to remove Mg salts and organic reagents) and subsequently dried by a stream of N_2 gas. The Si−CH_3 wafers were stored in N_2(g)-purged container and covered in aluminum foil to protect the surface from oxidation before any photoelectrochemical measurements or ALD deposition.

2.1.2. Atomic Layer Deposition (ALD) of Al_2O_3 Passivation Layer and Pt. Al_2O_3 passivation layers were deposited on CH_3-terminated Si(111) substrates by ALD using a Savannah S100 apparatus (Cambridge Nanotechnology, Inc.). The deposition of Al_2O_3 resulted from the reaction between trimethylaluminum (TMA, M_w = 72.09 g

DOI: 10.1021/acsami.5b00376
ACS Appl. Mater. Interfaces 2015, 7, 8572−8584

mol^{-1}, Sigma-Aldrich) with chromatography-grade H_2O. The temperature of the substrate and gas lines were kept at 150 °C, while the temperature of the TMA precursor container was kept at room temperature. Room temperature is sufficient for the highly volatile TMA to provide a steady state flux from source to reactor. High-purity N_2 (99.999%) was used for purging and as the carrier gas. Al_2O_3 films were deposited under 20 sccm of N_2 flow and base pressure of ∼0.4 Torr. During the ALD process, the TMA and H_2O pulse lengths were 0.015 s, and they were separated by 20 s of N_2 purge.

The Pt ALD was carried out on CH_3-terminated Si(111) or on Al_2O_3 deposited Si(111)−CH_3 wafers using the same Savannah S100 apparatus. The deposition of Pt results from the reaction of trimethyl(methylcyclopentadienyl)-platinum(IV), [(MeCp)Pt(Me)$_3$], M_w = 319.30 g mol^{-1}, Sigma-Aldrich) with high-purity O_2 (99.999%). The temperature of the substrate was kept at 240 °C while the Pt precursor container and gas lines were kept at 70 and 150 °C, respectively, to provide a steady state flux from source to reactor. High-purity N_2 (99.999%) was used for purging and as the carrier gas. Platinum ALD was performed under 20 sccm of N_2 flow and base pressure of ∼0.4 Torr. During the ALD process, the [(MeCp)Pt(Me)$_3$] and O_2 pulse lengths were 1 and 0.015 s, respectively, and they were separated by 5 s of N_2 purge.

2.2. Characterization of Si(111) Photoelectrode. XPS spectra were obtained using a commercial X-ray photoelectron spectrometer (Kratos Axis Ultra) with a monochromated Al Kα X-ray source ($h\nu$ = 1486.5 eV). The photoelectron takeoff angle was normal to sample surface and 45° with respect to the X-ray beam. The pressure of the analysis chamber was typically 2×10^{-9} Torr during measurement. Spectra were obtained by single sweep with a dwell time of 1200 ms (C and O), 2000 ms (Si), and 1600 ms (Al). A 300 × 700 μm^2 spot and 20 eV of pass energy with 0.1 eV resolution was used for all XPS measurements. The obtained spectra were analyzed with Casa XPS software (version 2.3.15, Casa Software, Ltd.) using 70% Gaussian and 30% Lorentzian function after subtraction of Shirley background. The binding energies of each spectrum were calibrated by Si 2p peak at 99.4 eV. From the XPS signal, the Al_2O_3 film thickness (t_{ox}) was calculated by using the following equation:

$$t_{ox} = \lambda \sin\theta \ln(R/R_\infty + 1) \quad (1)$$

where λ is the attenuation length of the photoelectrons, θ is the photoelectron takeoff angle (90°), R is the ratio I_{ox}/I_{Si} in the sample, R_∞ is the ratio I_{ox}/I_{Si} in a sample where the oxide film is greater than 10 nm thick.[25] The measured attenuation length and R_∞ values for thermally grown silicon oxide films can be applied to aluminum oxide deposited via atomic layer deposition in ultrathin oxide films (less than 4.5 nm) because such thin films only elicit minimal elastic photoelectron scattering. Thus, from the literature,[26,27] 2.96 nm and 0.91 were used for λ and R_∞, respectively.

The surface morphology of the Pt nanoparticles were determined by Quanta 650 SEM (FEI). For all analyses, the SEMs were operated at 30 kV and a 10 mm working distance with a secondary electron detector. Surface recombination velocity (SRV, S) was measured by observing carrier lifetimes using photoconductivity decay. Measurements were carried out using a contactless microwave conductivity apparatus with a 20 ns laser pulse (905 nm, OSRAM laser diode and ETX-10A-93 driver; Growth Equipment, Inc.). The concentration of charge carriers generated by a pulse laser was monitored as a function of time using reflected microwave radiation with a PIN diode. The carrier lifetimes (τ) were extracted by exponential decay fitting from obtained data, and the τ was then converted to S values using the following equation:[28]

$$\frac{1}{\tau} = \frac{1}{\tau_B} + \frac{2S}{d} \quad (2)$$

where τ is the measured lifetime, τ_B is the bulk lifetime, and d is the wafer thickness. For high-purity Si, the bulk carrier lifetime is much larger than the measured lifetime ($\tau_B^{-1} \ll \tau^{-1}$). Therefore, eq 1 can be simplified:[28]

$$S = \frac{d}{2\tau} \quad (3)$$

2.3. Electrochemistry. *2.3.1. Fabrication of Cell for Photoelectrochemical (PEC) Measurements.* The PEC properties of surface-modified samples were investigated using a WaveNow (Pine Research Instrumentation, USA) potentiostat. A three-electrode setup was utilized, with a Si working electrode, a Pt-wire (99.95%, Strem Chemicals, USA) counter electrode, and an Ag-wire quasi-reference electrode prepared from CHI112 (CH Instruments). The PEC cell was assembled as shown in Figure S1 (Supporting Information), and the wafer contacted according to known procedures:[9] a piece of copper tape (Electron Microscopy Sciences) was attached to a metal base for leading of working electrode. Before the sample was placed on the copper tape, the Si wafer was scratched using a diamond scribe, and Ga−In eutectic (99.99%, Alfa Aesar) was applied for ohmic contact. The ohmic contact and metal base were protected from electrolyte solution by an O-ring. The light active area defined by the diameter of the O-ring (0.6 cm) was 0.28 cm^2. This area was applied to calculate current density (mA cm^{-2}) after measurement. The light source used to simulate sunlight at 100 mW cm^{-2} was a 150 W Xe lamp (Newport, Co.) equipped with an AM1.5 solar filter (Newport, Co.).

2.3.2. PEC Characterization of Al_2O_3-Passivated Si(111)−CH_3 Substrates. Cyclic voltammetry (CV) was performed to evaluate the electrochemical properties of *n*-Si wafer at varying thicknesses of Al_2O_3 passivation layers both with and without Pt. For Nernstian CV response as well as stability testing, both acetonitrile and aqueous electrolyte solutions were prepared: 2 mM ferrocene (98%, Acros Organics) in 0.3 M $LiClO_4$ acetonitrile solution, and 3 mM ferrocenemethanol (Fc−OH, 97%, Sigma-Aldrich) in 0.3 M $LiClO_4$ aqueous solution. Before performing each CV scan, the electrolyte solution was degassed by N_2 bubbling for 30 min to remove dioxygen from the solution. All potentials of electrochemical results are shown as raw potential scale (vs Ag), and the redox potential of $Fc^{0/+}$ was +0.284 V vs Ag. All PEC measurements were performed at a standard scan rate of 100 mV s^{-1} (except for scan rate dependence, collected at 10−1000 mV s^{-1}).

2.3.3. Electrochemical impedance spectroscopy (EIS). EIS was carried out using an Autolab PGSTAT 128N (Metrohm, Netherlands) in a three-electrode configuration system identical to previous experimental setup. An acetonitrile solution containing 10 mM ferrocene and 0.5 M $LiClO_4$ were used for the electrolyte solution. The applied potential was 0 V vs Ag and frequency range was 10^5−10^1 Hz. The collected spectra were analyzed by the Nova 1.8 software (version 1.8.14) to fit and calculate the element values.

2.4. Simulation for Comparison with Experimental Results. Cyclic voltammograms were simulated using the model shown by eq 4, with $I\psi$ defined as the convolution integral shown by eq 5:[29]

$$\psi = [\Lambda(1-\theta)] \exp(\alpha\xi) [1 - I\psi - I\psi \exp(-\xi)] \quad (4)$$

$$I\psi = \pi^{-1/2} \int_0^\tau \psi(\eta)(\tau - \eta)^{-1/2} d\eta \quad (5)$$

and

$$\psi = \frac{i}{\left[FSc^{\circ}\left(\frac{D}{t_c}\right)^{1/2}\right]};\ \Lambda = k_{app}^{s,o}\left(\frac{t_c}{D}\right)^{1/2};\ \xi = -\left(\frac{F}{RT}\right)(E - E^{\circ});$$

$$\tau = \frac{t}{t_c};\ t_c = \frac{RT}{F\nu}$$

where ψ, Λ, ξ, τ, and t_c are the dimensionless current, kinetic parameter, voltage, time constant, and current time, respectively.[29] This model is for a single electron transfer reaction, according to the reaction listed below on disc type active sites:[29]

$$A + 1e \rightleftharpoons B \quad (6)$$

As stated by Amatore,[29] this model assumes that nonlinear diffusion effects occur near the surface of the electrode, and that beyond a

DOI: 10.1021/acsami.5b00376
ACS Appl. Mater. Interfaces 2015, 7, 8572−8584

distance of $L = 2R_0$ the diffusion is linear and semi-infinite. The model also assumes that the distance between two adjacent active sites, $2R_0$, is small compared to the thickness of the diffusion layer.[29] The solution to eq 5 was carried out numerically to obtain values of $I\psi(\xi) = x(at)$ using eq 7 from Nicholson and Shain:[30]

$$2\sqrt{\sigma}\,[X(1)\sqrt{n} + \sum_{i=1}^{n-1}\sqrt{n-i}\,[x(i+1) - x(i)]] = \frac{1}{1 + \gamma\theta S_{\sigma\lambda}} \quad (7)$$

Equation 7 was solved using Matlab with an integration width (δ) of 0.02. The solution to eq 7 is independent of the value of $\gamma\theta$ as long as the value of $\ln(\gamma\theta)$ remains above ~6.0.[31] A value of 6.5 was used for $\ln(\gamma\theta)$ in this simulation. The function $S_{\sigma\lambda}(\delta n)$ is defined as $\exp(-\delta n)$ and $\exp(\delta n - 2\delta\lambda)$ for the forward and backward sweeps, respectively.[30] The resulting equations were utilized to simulate cyclic voltammograms using Microsoft Excel. The fractional coverage of the blocking film, θ, was set to zero, which assumes that charge transfer can occur through the Al_2O_3 ultrathin film as long as the thickness remains below 50 Å. The parameters used for the simulation are summarized in Table 1. The general effects of modulating k_{app} in the trends of the CVs were visualized by selecting k_{app} values that varied from 1×10^{-3} to 1×10^{-8} cm s^{-1}; the simulation was unreliable at larger values of k_{app} due to the assumption of a significant blocking layer; simple Nernstian CVs were simulated in DigiElch (Gamry Instruments). The simulation of specific data sets was achieved using the MS Excel Solver Add-in to match the peak current density of the simulation at 100 mV s^{-1} to the experimentally observed current density at 100 mV s^{-1}; the experimental k_{app} values were thus obtained.

Table 1. Parameters for CV Simulation

parameter	value		
	0 cycles	10 cycles	30 cycles
active surface area of electrode (cm^2)	*ibid*	0.28	*ibid*
diffusion coefficient (cm^2 s^{-1})		2.3×10^{-5}	
concentration (mol L^{-1})		0.002	
scan rate (mV s^{-1})		25−1000	
temperature (K)		293.15	
transfer coefficient, α		0.5	
standard reduction potential (V)		−0.31	
apparent rate constant, $k_{app}^{s,o}$ (cm s^{-1})	~1×10^{-3}	~1×10^{-4}	~1×10^{-6}
surface coverage, θ		0	

3. RESULTS AND DISCUSSION

3.1. Characterization of Deposition Process on Si(111)|CH$_3$ to form Si(111)|CH$_3$|Al$_2$O$_3$.

3.1.1. XPS Characterization. Figure 1 shows the XPS spectra for the Si 2p and Al 2p regions on *n*-Si(111) wafers treated with increasing Al_2O_3 ALD cycles. The black curves in Figure 1a,b (Si and Al) represent the nascent Si(111)|CH$_3$ sample prior to Al_2O_3 ALD. The dark blue curve in each plot represents the sample following 30 cycles of Al_2O_3 ALD. To determine the deposition rate and growth mode of aluminum oxide during the ALD process, we analyzed the ratio between the sum of the Si^0 components and the peak areas of Al. Figure 1c shows the resulting calculated thickness of Al_2O_3 film as a function of ALD cycle. The thickness of the Al_2O_3 layer increased exponentially up to 15 ALD cycles, after which the film grew in linear fashion. Based on a report regarding ALD of metal nanoparticles,[32] the exponential increase represents the nucleation phase of the deposition (island growth), whereas a linear increase in thickness indicates the buildup of the bulk material (conformal growth).[32] Accordingly, the present data reflects an initial phase of 3D island growth (0−15 cycles), followed by a continuing phase conformal film (2D) growth after 15 cycles of ALD. This result agrees with the report of Puurunen et al.,[33] which showed that the $AlMe_3/H_2O$ ALD process on H-terminated Si(100) surface also produces an island-growth mode (as determined by TEM and LEIS). These authors ascribe this result not to the properties of the $AlMe_3/H_2O$ ALD process, but instead to the inherent use of the H-terminated surface as the substrate. Therefore, the analogous lack of nascent nucleation sites (e.g., oxides and hydroxides) on CH_3-terminated Si(111) is likely the reason for this initial growth mode in this work. From the linear region in Figure 1c, the deposition rate of ALD-Al_2O_3 was defined as 1.6 Å/cycle in this system.

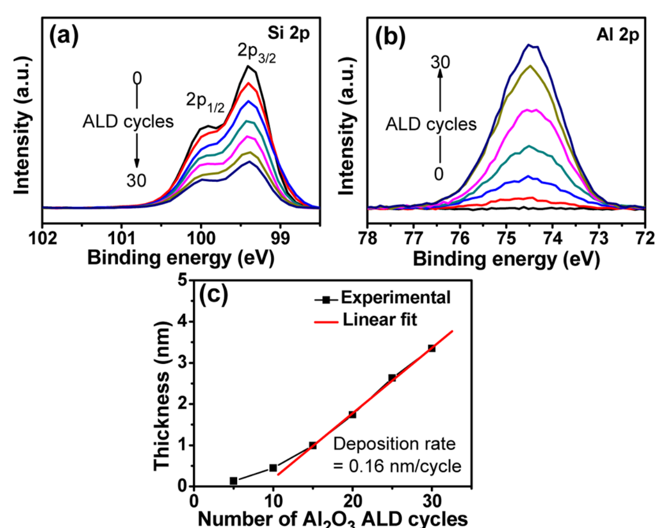

Figure 1. X-ray photoelectron spectra of (a) Si 2p and (b) Al 2p for the CH_3-terminated *n*-Si(111) photoelectrode depending on Al_2O_3 ALD cycles. Al_2O_3 growth curve as a function of ALD cycle (c).

For further quantitative analysis, the assigned atomic core levels for *n*-Si(111)|CH$_3$ and *n*-Si(111)|CH$_3$|Al$_2$O$_3$-30 are shown in Figure 2. As shown in Figure 2a, the Si 2p spectrum of CH_3-terminated *n*-Si sample without ALD showed two peaks at 99.37 and 99.97 eV (red dash), and the distance between peaks was 0.6 eV (red dot). The former and latter peaks are assigned to Si $2p_{3/2}$ and Si $2p_{1/2}$, respectively, corresponding to the typical position of Si−Si bond reported to be 99.4 ± 0.3 eV (Si $2p_{3/2}$).[34,35] The spectrum in the inset (50× magnification) in Figure 2a shows a Si−O signal from the CH_3-terminated Si surface, which represents a trace amount of oxidized or hydroxylated silicon surface (green dash-dot). A previous report delineates a method to quantify atop Si−X (X = CH_3, O, etc.) sites using the Si signals according to the photoelectron takeoff angle, Si escape depth, and density of Si atoms. For the parameters in our experiment ($d_{esc\text{-}Si}$ = 1.6 nm),[8] the surface oxide (Si−O) content is calculated to be $I_{Si-O}/I_{Si-bulk} = 0.005$, corresponding to ≤0.5% oxide surface content. On the basis of this experimental value and the previously reported STM imaging of ~100% methylated Si(111) prepared by the same procedure,[36] we can reasonably conclude ~99.5% (i.e., $1 - \phi_{Si-O}$) surface coverage of Si(111)−CH$_3$. This is supported by the C 1s XPS data discussed below.

Figure 2b also shows the C 1s core features. The C 1s signal of *n*-Si(111)|CH$_3$ was fit to three peaks (or four peaks on the Al_2O_3-deposited sample) and indicates contaminants from

DOI: 10.1021/acsami.5b00376
ACS Appl. Mater. Interfaces 2015, 7, 8572−8584

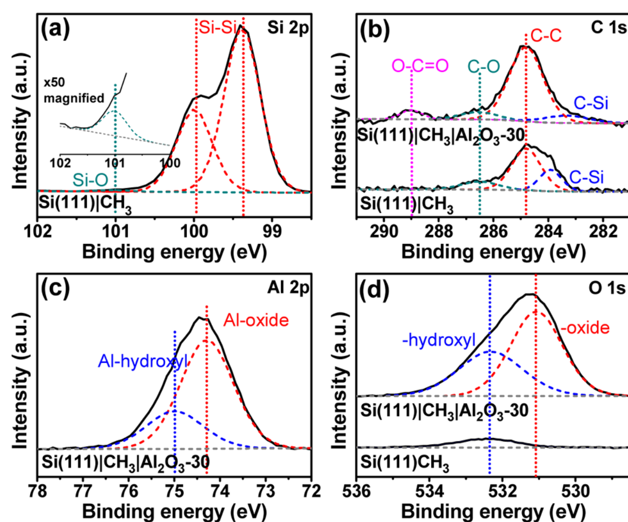

Figure 2. X-ray photoelectron spectra of (a) Si 2p, (b) C 1s, (c) Al 2p, and (d) O 1s for the CH_3-terminated *n*-Si(111) photoelectrodes with and without Al_2O_3. The dashed lines show a fitted peak and dot lines are representative for a position of each peaks.

exposure to ambient air: C−C (at 284.8 eV), C−O (at 286.5 eV), and O−C=O (at 289.0 eV).[37,38] The peak at 283.9 eV of *n*-Si(111)|CH_3 is representative of the carbon of the methyl group that is directly bonded to the atop Si sites (C−Si).[8,39] Indeed, the quantification of the C−Si portion of the C 1s signal ($I_{C-Si}/I_{Si-bulk}$ = 0.45) is consistent with the benchmark value established by the original researchers ($I_{C-Si}/I_{Si-bulk}$ = 0.52).[8] After Al_2O_3 ALD deposition, the C−Si bond position shifted by 0.68 to 283.24 eV. After more than five cycles of Al_2O_3 ALD, the peak at 101.01 eV (Si−O bond) was not detectable (magnification not shown), suggesting no SiO_x formation during ALD growth and a high extent of conformal coverage and passivation by the Al_2O_3 layers.

Figure 2c,d shows a detailed views of the Al 2p and O 1s core level XPS spectra on the *n*-Si(111)|CH_3|Al_2O_3-30 sample. Interestingly, the Al 2p region could be assigned as two separate species. The Al 2p core level (Figure 2c) was assigned two peaks at 74.3 eV (red dash and dot) and at 75.0 eV (blue dash and dot) corresponding to the typical positions of pure Al_2O_3 and terminal Al−OH groups, respectively.[40,41] As shown in Figure 2d, the O 1s spectrum of *n*-Si(111)|CH_3|Al_2O_3-30 was also separated by two peaks. The main component having lower binding energy of 531.08 eV is related to the oxide ion of the Al_2O_3.[40] Consistent with the Al 2p spectra, the higher binding energy peak of 532.36 eV can be attributed to the hydroxyl group (Al−OH), or to contaminants (carboxyls and/or carbonates) as mentioned in C 1s core level assignment. Compared with O 1s core level peak position of the *n*-Si(111)|CH_3 sample (Figure 2d), this assignment appears correct: the O/Al atomic ratio calculated by the O_{oxide} and Al_{oxide} components was 1.42, in agreement with the stoichiometry of Al_2O_3 (O/Al ratio of 1.5).[40] At very thin film thicknesses, the surface Al−O_x species will also comprise a significant portion of the Al 2p signal. For example, surface associated $Al(OH)_3$ would afford a rigid 3:1 ratio, while a surface-bound $Al(O_{bulk})_n(OH_{surf})_m$ would on the whole produce *a* < 3:1 ratio due to lack of capping Al atoms. Considering the observed the XPS ratio of $O_{hydroxyl}/Al_{hydroxyl}$ was 2.3:1, one can deduce that this signal emanates from the surface Al−OH species.

3.1.2. Current-Thickness Dependence. Cyclic voltammetry was used to evaluate photoelectrochemical performance of CH_3-terminated Si(111) substrates depending on the thickness of the Al_2O_3 layers. The *n*-Si(111)|CH_3 was evaluated by the reversible oxidation of ferrocene (2 mM) in 0.3 M $LiClO_4$ acetonitrile solution with a potential range between −0.8 V and +0.3 V vs Ag. Ferrocene has been widely used as an internal standard, and the redox potential of Fc/Fc^+ (0.64 V vs NHE) is located within the band gap of silicon.[42] Under irradiation, the holes generated at the valence band of *n*-Si(111) were scavenged by oxidation of ferrocene, and the maximum current of the ensuing oxidation wave (J_{ox}, see inset of Figure 3) was

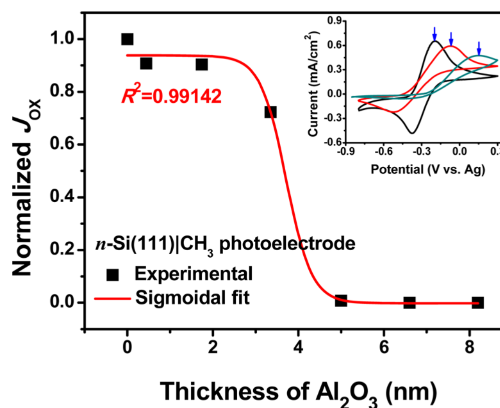

Figure 3. Effect of Al_2O_3 thickness on maximum current (J_{ox}) of oxidation for CH_3-terminated *n*-Si(111) substrate with 2 mM ferrocene ($Fc^{0/+}$) in 0.3 M $LiClO_4$ acetonitrile solution. The inset figure shows the J_{ox} features for *n*-type semiconductor. All data were collected at 100 mV s^{-1} scan rate.

used as a metric for comparing performance among devices. The redox potential of ferrocene/ferrocenium ($E_{1/2}$) and the J_{ox} of bare *n*-Si(111)|CH_3 were approximately −0.3 V (vs Ag) and 0.65 mA cm^{-2}, respectively, and the $E_{1/2}$ value was largely unaffected with increasing of Al_2O_3 ALD layers. The sigmoidally decreasing value of J_{ox} obtained upon increasing the number of Al_2O_3 ALD cycles is displayed in Figure 3. Up to 18 cycles, the J_{ox} value remained almost constant with a magnitude close to bare *n*-Si(111)|CH_3. The observed current then decreased precipitously between 18 and 50 Å, and beyond 50 Å of Al_2O_3 deposition, the current was negligible, indicating that electron transfer is severely inhibited between the bulk Si and the electrolyte in the PEC cell. Although this simple treatment does not give exact insight into the structural and electronic properties of the Al_2O_3 layer at less than 30 cycles (∼34 Å), one may conclude that (along with the XPS result in Figure 1c) the Si surface is incompletely covered with Al_2O_3 due to the island growth mode observed during the initial ALD cycles. Indeed, Bard et al. recently reported a similar sigmoidal effect resulting from ALD-TiO_2 passivation on an ITO substrate.[43] At thicknesses of 1−3 nm, the chronoamperometric current was dramatically decreased as a function of increasing ALD-TiO_2 cycles. This phenomenon was reported to be caused by a gradual covering of pinhole sites dependent on the number of ALD cycles. This ALD effect on ITO was interpreted as not being caused by a tunneling effect,[43] and our current−thickness plot appears to follow the same sigmoidal trend. In contrast to ITO (roughness factor of ∼1−5 nm), the atomically flat Si(111) surface should be less prone to pinhole formation; however, this cannot be excluded in the present study. In the

DOI: 10.1021/acsami.5b00376
ACS Appl. Mater. Interfaces 2015, 7, 8572−8584

initial ALD cycles (<15 cycles), the metal oxide coverage increases but is not effective to decrease J_{ox} (this will be discussed in the next section), while at intermediate ALD cycles ($15 < x < 40$), the current is significantly decreased, possibly suggesting that the pinholes are removed. At greater than 40 ALD cycles (estimated ∼50 Å of Al_2O_3), the Si surface is covered with a conformal film of Al_2O_3 that is postulated to be free of defects, pinholes for electrolyte diffusion, or other channels available for fast electron transfer. We can thus confirm that such a thin layer of Al_2O_3 (50−82 cycles) can inhibit direct contact between the semiconductor surface and electrolyte.

3.1.3. Electrochemical Impedance Spectroscopy (EIS). To gain more insight into the electronic effects of thin Al_2O_3 films on the *n*-Si(111)|CH_3|Al_2O_3 samples, we have utilized EIS, which has been widely used to characterize the passivation layer of surfaces in a nondestructive manner. In this measurement, the high frequency region ($f > 10^3$ Hz) corresponds to the series resistance (R_s), the middle frequency region ($10^3 > f > 10^0$ Hz) corresponds to processes related to charge-transfer reaction at the electrode/electrolyte interface, and the low-frequency region ($f < 10^0$ Hz) corresponds to factors involving the diffusion properties of the electrolyte and redox couple.[44] In this work, the low-frequency region ($f < 10^0$ Hz) is not reported due to high variability and low signal/noise ratios. Additionally, the same electrolyte solution was used in each measurement, and thus, the assumption that the diffusion parameters for each sample is invariant is valid.

Figure 4 shows the impedance data as Bode plots (phase angle vs log(f)) of the *n*-Si(111)|CH_3 coated with increasing

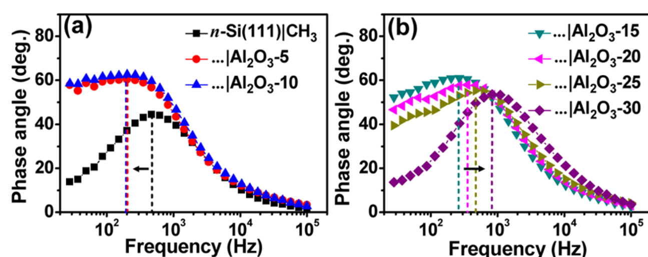

Figure 4. Bode phase plots of electrochemical impedance spectroscopy for CH_3-terminated *n*-Si(111) depending on Al_2O_3 ALD cycles: (a) 0−10 and (b) 15−30 ALD cycles.

Al_2O_3 thicknesses. As shown in Figure 4a, the peak frequency of Si substrates functionalized with very thin Al_2O_3 layers (5−10 cycles; 1.3−4.5 Å) were shifted to lower frequencies. In contrast, during formation of the conformal film (15−30 cycles; 10−34 Å), a trend of increasing characteristic frequencies was observed (Figure 4b). This region of capacitance is inversely proportional to the Al_2O_3 thickness, as oppositely charged plates at long distances lose their capacitive power. These contrasting results can be interpreted in the following way. The observed capacitative effect is attributable to two factors: (1) Al or O vacancies in the nascent (defect-containing) ultrathin film,[12] and (2) increased photoexcited electron lifetime[45] at the Si|Al_2O_3|electrolyte multiface. First, Dingemans and Kessels have elaborated on the effects of Al_2O_3 thickness on the fidelity of Al_2O_3 films (i.e., occupancy of Al and O sites).[12] These authors (and others[46,47]) note that very thin films of Al_2O_3 have high concentrations of Al and O vacancies. These charge-unbalanced sites give rise to field effects (Q), which can be correlated with observed capacitance. As the capacitance of the Si−CH_3|Al_2O_3 junction will be related to the concentration of defect sites inside the Al_2O_3 layer, it thus may be expected that the thinner Al_2O_3 layers will exhibit more ideal capacitive behavior. Second, Yuan and co-workers have reported on the EIS effect of ALD Al_2O_3 on TiO_2 nanotubes, wherein the shift in the peak phase angle to lower frequencies at a low number of ALD cycles (5−10) was attributed to increased lifetime of photoexcited electrons at the TiO_2|Al_2O_3|I^-/I_3^- junction.[45] However, the effect of higher number of ALD cycles was not reported in this system.

3.2. Cyclic Voltammetry Behavior and Simulation of Electron Transport across Si(111)|CH_3 and Si(111)|CH_3|Al_2O_3. *3.2.1. Rationale.* In the previous sections, up to a sub-2 nm thick layer, the charge-transfer rate is sufficiently fast to achieve reasonable J_{ox} values (100 mV s^{-1}) as compared to electrodes without Al_2O_3 treatment. We thus wished to further explore the time-dependent phenomena by the simple means of modulating the CV scan rate. In simple terms, drastic effects on CV shape may be anticipated when the scan rate approximates or exceeds the rate of electron transfer across the Si|CH_3|Al_2O_3 interface. Below, we present CVs at varying scan rates on devices with increasing Al_2O_3 thicknesses.

3.2.2. Experimental Data in MeCN. The CV sweep rate dependence on a bare *n*-Si(111)|CH_3 photoelectrode under 1 sun illumination using 2 mM Fc in MeCN (0.3 M $LiClO_4$) is shown in Figure 5a. Plots of the maximum current at each peak (J_{ox}, Figure 5e; J_{red}, Figure 5f) versus square root scan rate exhibit a linear relationship for the bare and Al_2O_3 coated samples, confirming the homogeneous nature of the redox processes. Per standard analysis, the slope of the resulting data

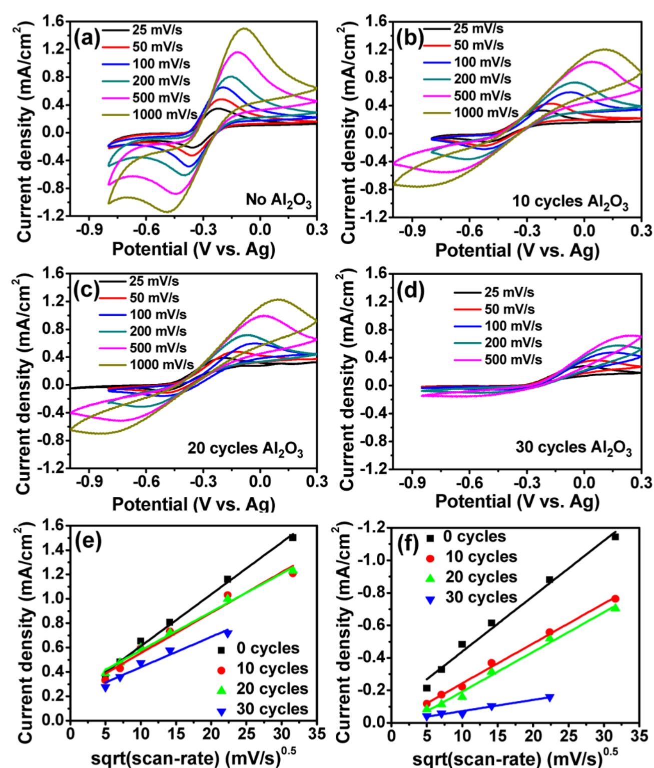

Figure 5. CV scans for (a) *n*-Si(111)|CH_3, (b) *n*-Si(111)|CH_3|Al_2O_3-10, (c) *n*-Si(111)|CH_3|Al_2O_3-20, and (d) *n*-Si(111)|CH_3|Al_2O_3-30 using 2 mM ferrocene in 0.3 M $LiClO_4$ acetonitrile solution as the electrolyte. Plots of the peak photocurrent density of the (e) oxidation peak and (f) reduction peak versus square root of scan-rate.

DOI: 10.1021/acsami.5b00376
ACS Appl. Mater. Interfaces 2015, 7, 8572−8584

can be taken as an aggregate constant comprised of D_{expt} and k_{app}. At an unblocked electrode, the term simplifies to represent only the diffusion constant of the redox couple in a given electrolyte, in this case affording $D_{Fc/MeCN} = 1.02 \times 10^{-5}$ ($D_{Lit} = 2.3 \times 10^{-5}$ on Au or GC electrodes).[48] Such close agreement suggests that the organic monolayer of methyl groups does not provide any substantial inhibitory properties in the electron transport (ET) process.

Upon deposition of a very thin film of Al_2O_3 (10 cycles, ~4.5 Å), the resulting CV (Figure 5b) exhibits a broadened anodic feature of slightly reduced current, as well as a broadened cathodic sweep of greatly reduced current. The deposition of an additional 10 cycles of ALD (~18 Å total Al_2O_3), results in CVs (Figure 5c) that are nearly identical as compared with the 10-cycle sample (vide infra for interpretation). The 30-cycle ALD sample Si|CH_3|Al_2O_3-30 (~34 Å total Al_2O_3) continues to exhibit a broadening trend, with further deviation from Nernstian behavior, especially in the return cathodic sweep. Beyond 34 Å of Al_2O_3, minimal current was observed due to the increasingly resistive Al_2O_3 film. It has been previously estimated that the maximum tunneling distance through an insulating material is ~20 Å,[20] beyond which tunneling does not occur or requires special conditions. The results herein are thus in line with previous reports.

3.2.3. Simulation of CVs in MeCN. Despite the 3D growth mode suggested by the XPS and EIS data, the observed CV shapes are (at first appearance) characteristic of a conformal, resistive, and electroactive layer that gives rise to a uniform slowing of electron transfer across the quasi-insulating layer. For example, the XPS and EIS data suggest 3D island growth at very low cycles of Al_2O_3 ALD, which could result simply in a decrease in the electroactive surface area of the photoelectrode (i.e., lower J_{max}, but similar operating potentials). However, as few as 10 ALD cycles effects a dramatic change in the operating potentials during the CV experiment, and such broadening of the Nernstian wave is consistent with slow electron transport across a resistive film. In an effort to quantify this apparent paradox, we first pursued a kinetic analysis of electron transfer at varying Al_2O_3 thicknesses.

The observed trend of broadening CV features is due to a decrease of the apparent standard rate constant,[49] which has been described in detail conceptually, mathematically, and visually several decades ago by Amatore et al.,[29] as well as Nicholson and Shain.[30] Overall, in cases where the Al_2O_3 layer is very thin on the *n*-Si|CH_3|Al_2O_3 devices, the experimental and simulated CV data herein is consistent with the known model of fast e^- transfer/slow sweep rates (i.e., the rate of charge transport exceeds the electrons supplied by the sweep rate). For thicker Al_2O_3 layers, the electrochemical regime changes to one of slow e^- transfer/fast sweep rates (i.e., charge transport is slower than the electrons supplied by the sweep rate). More detailed experimental observations are described below.

It is important to note that in all cases the current decreases for the reduction event, to a greater extent than the current diminishes for the oxidation event (Figure 5, panel e versus panel f). This trend can be explained by two factors: (1) the slowing of ET across the quasi-insulating layer in the anodic sweep, and (2) the relatively fast diffusion coefficient of ferrocene. That is, if diffusion is fast, a majority of ferrocenium that is formed during the oxidation sweep will exit the diffusion layer near the semiconductor surface before the return reduction wave occurs. This process is exacerbated/highlighted by the enforced slow ET during both the anodic and cathodic waves. Also, the oxidation peak shifts to more anodic potentials and the reduction peak shifts to more cathodic potentials.[49] It is important to note that these observations will only be observed using a redox couple with a large diffusion coefficient; otherwise, diffusion limitations will result in kinetic effects not being observed, or at least minimized (see aqueous CV measurements in section 3.3).

The experimental data is not exclusively consistent with an island growth model of Al_2O_3, in which defects or pinholes are the dominant factor beyond our first measured points at five cycles of ALD (~1.3 Å Al_2O_3). In electrochemical terms, the island growth model is only analytically observable if the islands were of sufficient thickness to be completely blocking (i.e., >30−40 Å of Al_2O_3), such that only the electro-active surface area of the electrode was reduced (diminishing J_{max}), but without any change in the k_{ET} value (i.e., no change in ΔE_p). In this case, the ΔE_p value is modulated even at low ALD cycles, most likely because the islands are of sufficient thickness to slow ET, but not to completely block it. Thus, the resulting CV data is a composite measurement that entails both concomitant effects (k_{ET} slowing, and surface area decreasing). Additionally, this result might be expected because unlike glassy carbon, graphite or HOPG electrodes (which exhibit pinholes and require much higher ALD cycles to passivate), the Si(111) surface is atomically flat and possesses essentially no roughness factor.

Based on the conformal growth premise, we more precisely simulated the experimental CVs (Figure 6: 0, 10, and 30 cycles, side-by-side experiment and simulation) by matching the peak anodic current density of the experimental data at 100 mV s^{-1} to that of the simulation under the same conditions. (The detailed simulated CVs under further varying conditions are available in Figures S3 and S4, Supporting Information.) The simulated rate constant of the sample with 0 cycles of Al_2O_3 may not be precise because the model is only applicable for slow kinetics ($k_{app}^{s,o} < 10^{-3}$ cm s^{-1}) at electrodes with blocking layers. The simulations thus predict a trend of rapidly decreasing k_{app} values (see Table 2), progressing from the unblocked *n*-Si(111)|CH_3 ($k_{app} = 2.2 \times 10^{-2}$ cm s^{-1}), to the ~10 ALD-Al_2O_3 film ($k_{app} = 2.7 \times 10^{-4}$ cm s^{-1}), and finally to the ~30 ALD-Al_2O_3 film ($k_{app} = 2.3 \times 10^{-7}$ cm s^{-1}). While the middle values are consistent with a simple slow ET across a quasi-insulating layer (typically $1 \times 10^{-2} > k_{app} > 1 \times 10^{-5}$ cm s^{-1}),[50,51] the latter value is consistent with reported k values associated with a tunneling processes through an inert matrix.[49]

3.3. Stability Test of Si(111)|CH_3 and Si(111)|CH_3|Al_2O_3. *3.3.1. Increased Potential Window.* In the cyclic voltammetry experiments described above, we determined a broadly applicable window of stability for *n*-Si(111)|CH_3 electrodes with and without Al_2O_3 to be approximately −1.0 to +0.3 V vs Ag in MeCN electrolyte. In this experiment, we expanded the anodic window to +0.5 V vs Ag to determine the ability of the Al_2O_3 films to protect against corrosion processes (SiO_x and surface defect formation). Figure 7 shows CVs of *n*-Si(111)|CH_3 and *n*-Si(111)|CH_3|Al_2O_3 samples measured in 0.3 M $LiClO_4$ acetonitrile solution with 2 mM ferrocene. The bare sample (Figure 7a) exhibits a marked shift in both the anodic and cathodic peaks, indicating the occurrence of a corrosion process and SiO_x formation. These samples were permanently compromised, and they did not retain the original CV shape upon retesting after agitation of the diffusion layer. The Al_2O_3-30 passivated sample also showed a decrease in

DOI: 10.1021/acsami.5b00376
ACS Appl. Mater. Interfaces 2015, 7, 8572−8584

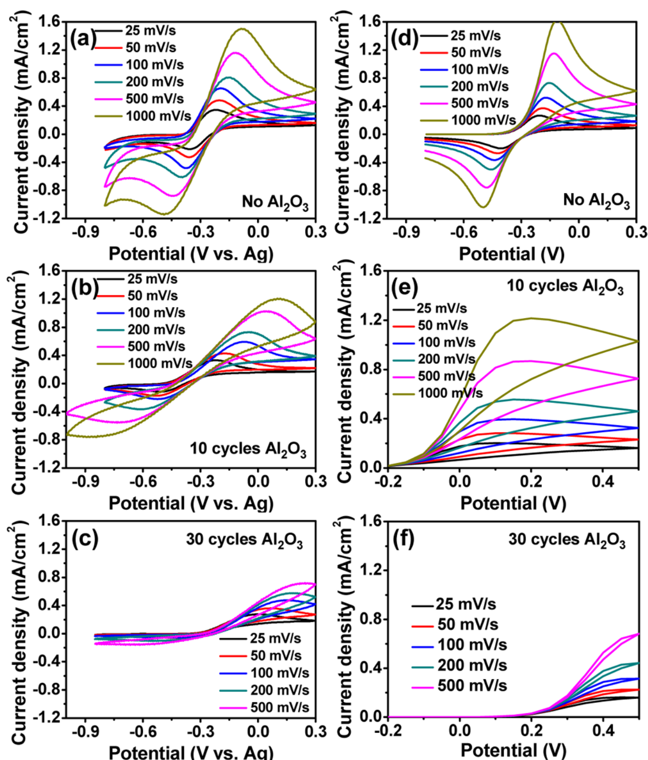

Figure 6. Side-by-side comparison of the shapes of (a−c) experimental and (d−f) simulated cyclic voltammograms as determined for 2 mM ferrocene in 0.3 M $LiClO_4$/acetonitrile as the electrolyte solution. Simulated cyclic voltammograms depending on apparent rate constant were obtained by the parameters in Table 1 with various rate constants: (d) 1×10^{-3} cm s^{-1}, (e) 1×10^{-4} cm s^{-1}, and (f) 1×10^{-6} cm s^{-1}.

Table 2. Simulated Rate Constants for *n*-Si(111)|CH_3, and *n*-Si(111)|CH_3|Al_2O_3 using 2 mM Ferroceone in 0.3 M Lithium Perchlorate/Acetonitrile As the Electrolyte Solution

cycles of Al_2O_3	thickness (Å)	simulated rate constant (cm s^{-1})
0	0	2.23×10^{-2}
10	4.5	2.71×10^{-4}
20	18	4.48×10^{-4}
30	34	2.32×10^{-7}

current for both the anodic and cathodic peaks (Figure 7c), but without the shift in peak potentials as observed on the bare sample. However, retesting of the same substrate after simple agitation of the electrolyte solution (Figure 7d) regenerated the J_{max} and operating potentials of the original scan, indicating the observed changes over consecutive CV scans are not due to any corrosion processes. Thus, the diminishing J_{max} values in consecutive CV scans (no agitation of the electrolyte) are attributed simply to consumption of the ferrocene redox couple in the diffusion layer during consecutive CV scans. The samples of 10 and 20 cycles ALD-Al_2O_3 exhibited CV behavior intermediate between the bare and Al_2O_3-30 cases. Thus, it is clear that the 30-cycle Al_2O_3 layer protects the Si surface from oxidation at moderately positive potentials (+0.5 V vs Ag) and that at this thickness the Si(111)|CH_3 surface is likely isolated from directly contacting the electrolyte solution in a pinhole-free blocking regime.

3.3.2. Aqueous Stabilization by Al_2O_3 Films. Furthermore, *n*-Si electrodes treated with Al_2O_3 layers showed increased

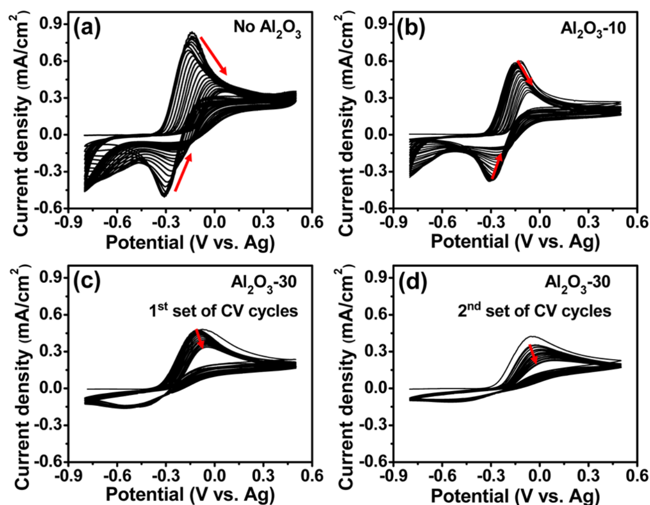

Figure 7. Cyclic voltammograms obtained with an increased potential window in 2 mM ferrocene with 0.3 M $LiClO_4$ in acetonitrile. (a) *n*-Si(111)|CH_3, (b) *n*-Si(111)|CH_3|Al_2O_3-10, (c) 1st set of *n*-Si(111)|CH_3|Al_2O_3-30, and (d) 2nd set of *n*-Si(111)|CH_3|Al_2O_3-30.

stability in aqueous solution. Due to the high fidelity of the methylation procedure, all *n*-Si(111) samples [including the bare *n*-Si(111)|CH_3 sample] showed reproducible behavior (>10−20 CV scans) using ferrocenemethanol (Fc−OH) redox couple in aqueous electrolyte (0.3 M $LiClO_4$) at moderate potentials (−1.0 to +0.2 V vs Ag). As shown in Figure 8,

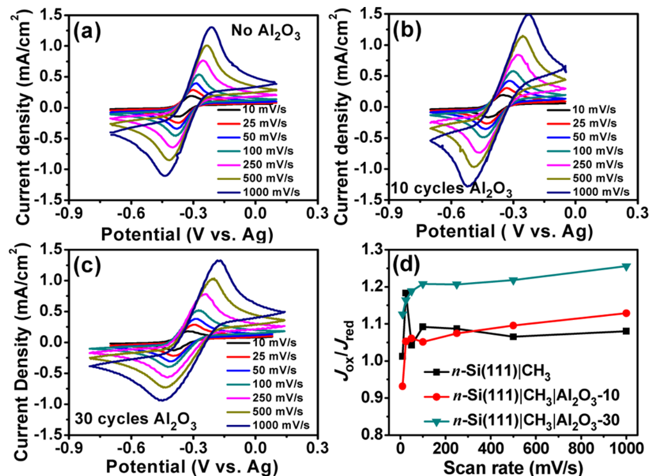

Figure 8. Cyclic voltammograms for (a) *n*-Si(111)|CH_3 and (b and c) *n*-Si(111)|CH_3|Al_2O_3-*x* depending on scan rate obtained in aqueous solution containing ferrocenemethanol (3 mM) and $LiClO_4$ (0.3 M) as supporting electrolyte. (d) Maximum peak current ratio (J_{ox}/J_{red}) depending on Al_2O_3 thickness.

samples spanning from the bare *n*-Si(111)|CH_3 to the fully protected *n*-Si(111)|CH_3|Al_2O_3-30 exhibited Nernstian CV behavior without any indication of corrosion or device degradation.

Quite different from experiments performed in MeCN with ferrocene, the shape of CVs were apparently identical, even as the thickness of the Al_2O_3 layer was increased. The primary factor is likely the smaller diffusion constant of Fc−OH in H_2O ($D_{expt} = 2.13 \times 10^{-6}$ cm^2 s^{-1}; $D_{Lit} = 7.8 \times 10^{-6}$ cm^2 s^{-1}) versus that of Fc in MeCN ($D_{expt} = 1.02 \times 10^{-5}$ cm^2 s^{-1}; $D_{Lit} = 2.3 \times 10^{-5}$ cm^2 s^{-1}).[48,52] That is, the longer residency time of the

DOI: 10.1021/acsami.5b00376
ACS Appl. Mater. Interfaces 2015, 7, 8572−8584

electro-generated Fc−OH$^+$ within the diffusion layer allows for more reversible behavior.

A more precise analysis of the effect of Al_2O_3 film thickness on CV behavior may be illustrated by plotting the maximum peak current ratio (J_{ox}/J_{red}) versus Al_2O_3 thickness (Figure 8d). From this plot, it is evident that small changes in the peak current do in fact occur, primarily due to a decreasing J_{red} value: that is, thicker Al_2O_3 → slower k_{ET} → more escape time for Fc−OH$^+$ out of diffusion layer, resulting in lower J_{red}. This diminished J_{red} value, however, does not deviate enough from Nernstian behavior to attempt meaningful CV simulations using the conformal resistive layer equations discussed above regarding the Fc/MeCN measurements. Notably, beyond 50 Å of Al_2O_3 (40 cycles ALD) thickness, the CV signal in H_2O was abolished; no intermediate case that exhibited CV broadening was observed. Overall, it is evident that the choice of electrolyte and redox couple is essential to experimentally determine k_{app} values for the quasi-insulating layers; such determination was not possible for our experiments in the case of Fc−OH/H_2O due to the retention of near-Nernstian behavior.

3.3.3. XPS Analysis after PEC Operation. To demonstrate the passivating effect of Al_2O_3 layers, XPS analyses of two *n*-type samples after the PEC/Fc experiment were performed. Figure 9 shows both the original XPS spectrum and the post-PEC XPS spectrum for two sets: the *n*-Si(111)|CH_3 and the *n*-Si(111)|CH_3|Al_2O_3-10 sample. For the comparison, intensity of the XPS signals were normalized. On the bare *n*-Si(111)|CH_3 sample (Figure 9a, red line), a notable feature is observed as a broad peak at 101.5−104.5 eV and is ascribed to the well-known silicon oxide feature (SiO_2, at 103 ± 0.3 eV).[53,54] As shown in Figure 9a, the XPS spectrum obtained after CV scans (red line) revealed not only SiO_2, but also higher intensity in the region between 100.5 and 101.5 eV comparing to the pre-CV XPS spectrum (black line). These features are assigned as the suboxides such as Si_2O and Si_2O_3 (Figure S5, Supporting Information). This oxidized state of *n*-Si(111)|CH_3 sample was presumably caused by trace dioxygen and water in the MeCN electrolyte, as well as through exposure to ambient air. By comparison, the same SiO_x feature on the protected *n*-Si(111)|CH_3|Al_2O_3-10 samples was nearly absent, and the sample does not exhibit any observable suboxides (Si_2O, SiO; Figure S5, Supporting Information). The atomic fraction of Si-oxide/Si-total for *n*-Si(111)|CH_3|Al_2O_3-10 was a relatively low 5.58% (approximately 0.5 monolayer), whereas the quantified value for the bare *n*-Si(111)|CH_3 sample was much higher (22.67%, 4−5 monolayers). Overall, these results demonstrate the marked passivation effects of the very thin film of Al_2O_3 on the Si surface during ambient storage and anodic device operation (Fc/Fc$^+$ in MeCN, +0.5 V vs Ag).

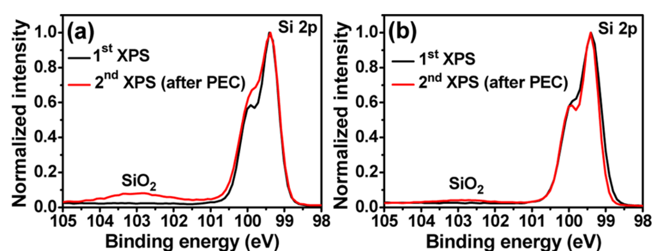

Figure 9. Chemical stability test as determined by XPS for (a) *n*-Si(111)|CH_3 and (b) *n*-Si(111)|CH_3|Al_2O_3-10 obtained by X-ray photoelectron spectroscopy. The black lines representing the as-prepared samples *n*-Si(111)|CH_3 and *n*-Si(111)|CH_3|Al_2O_3-10 were reproduced from Figure 1a. The red lines represent XPS spectra derived from samples used for electrochemical analysis.

3.3.4. Surface Recombination Velocity (SRV). To ensure SRV values that were representative of functional PEC devices, we performed the measurements on the *n*-doped wafers (1−10 Ω·cm resistivity). Thus, the values reported here are not comparable to those reported for intrinsic Si (much longer lifetimes). Nonetheless, the comparisons among the various etching/methylation/ALD treatments below highlight the important differences.

The carrier lifetime decay curves for each surface-functionalized sample is shown in Figure 10. A sample of freshly HF etched H-terminated *n*-Si(111) showed a charge carrier lifetime τ = 2.0 μs, and a corresponding SRV value of S = 8770 cm s^{-1}, which is considerably enhanced compared to the native hydroxyl-terminated *n*-Si(111) surface (τ = 1.2 μs; S = 14 000 cm s^{-1}). The methyl-terminated *n*-Si(111) surface showed a much longer charge carrier lifetime of 4.4 μs (S = 3950 cm s^{-1}), and the Al_2O_3 treated sample *n*-Si(111)|CH_3|Al_2O_3-15 surface exhibited an identical SRV value (4.2 μs, S = 4170 cm s^{-1}) by comparison.

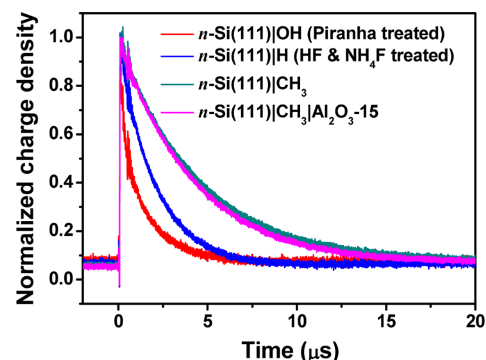

Figure 10. Time-resolved photoconductivity decay for *n*-Si(111)|CH_3 electrodes depending on the type surface functionalization. For the eidetic comparison, the *y* axis for each trace was normalized.

3.3.5. Thermal Stability prior to Pt ALD. Prior to our investigation of a platinum ALD process (next section), it was necessary to evaluate the competency of the photoelectrodes following a heat treatment (due to Pt ALD > 200 °C, versus Al_2O_3 ALD ≈ 150 °C). Samples for Pt catalyst deposition, namely *n*-Si(111)|CH_3 and *n*-Si(111)|CH_3|Al_2O_3-15, were placed in the ALD chamber (Savannah S100) and maintained at 250 °C for 10 min. The samples were then tested by photoelectrochemical measurements in 0.3 M $LiClO_4$ acetonitrile with 2 mM ferrocene. The bare *n*-Si(111)|CH_3 sample (Figure 11a) treated at 250 °C revealed a slight shift of redox potential ($E_{1/2}$) to negative and a decrease of both J_{ox} and J_{red}. This indicates the decompostion of the surface-functionalized organic layer by the thermal treatment. In contrast, the *n*-Si(111)|CH_3|Al_2O_3-15 sample showed remarkably stable photoelectrochemical behavior ($E_{1/2}$ and J_{redox}) in the before/after thermal treatment (Figure 11b). Thus, it is apparent that the Al_2O_3 dielectric layer exhibits an extent of thermal protection, as well. And although the bare *n*-Si(111)|CH_3 sample resists decomposition at the temperature of 250 °C for 10 min, we cannot ensure stability during the entire Pt ALD process, because the ∼200 cycles required for deposition takes ∼40 min. Nonetheless, as a result of this temperature stability test, the

DOI: 10.1021/acsami.5b00376
ACS Appl. Mater. Interfaces 2015, 7, 8572−8584

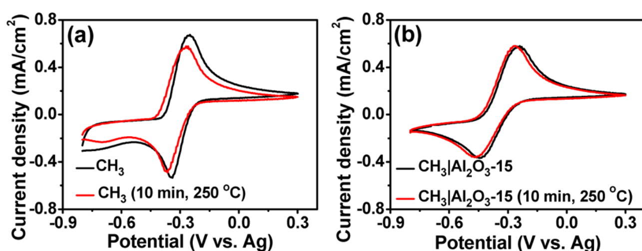

Figure 11. Cyclic voltammograms for (a) n-Si(111)|CH_3 and (b) n-Si(111)|CH_3|Al_2O_3-15 photoelectrodes before and after thermal treatment. Each sample was stored under vacuum in the ALD chamber for 10 min at 250 °C.

240 °C process was chosen in the ensuing experiments for Pt ALD.

3.4. Enhanced Electron Transport through a Semiconductor/Insulator/Metal (SIM) Architecture.

3.4.1. Pt Deposition by ALD. To complete the construction of a fully passivated and functional device, we wished to enhance the extent of electron transfer through films that were beyond the threshold limit of conformal growth as determined by XPS and EIS (~30−40 Å). As noted in the Introduction, the deposition of metallic entities (films or nanoparticles) has been reported to "rescue" the electron transport behavior of thin, insulating films. As such, we pursued the deposition of a model metallic system, platinum, on the n-Si|CH_3|Al_2O_3 substrates. The deposition of Pt is conventionally achieved using plasma as the counter-reactant during ALD processes.[55] However, the highly reactive plasma is not compatible with the organic monolayer of the CH_3-terminated Si substrate. A recent report of an alternative mode of Pt deposition utilizing O_2 as counter-reactant provided a promising path toward Pt deposition in this system.[23,56] The platinum precursor [(MeCp)Pt(CH_3)$_3$] exhibits deposition behavior in concert with O_2 as pulsing reagent at higher temperatures with slower rates (compared to the plasma-based process) and longer initiation times (270 °C, 0.45 Å/cycle, 25−75 cycles for initiation) as compared with the standard recipe for Al_2O_3 (150 °C, 1−1.5 Å/cycle, no initiation phase). Based on the above stability tests on bare and Al_2O_3-protected n-Si(111) electrodes, we selected a moderate temperature (240 °C) in conjunction with a higher number of cycles (150−200). Previous reports by others showed that this platinum ALD method deposits nanoparticles on the substrate, although the lag phase of Pt deposition depends greatly on individual experimental conditions (substrate, temperature, pulse time, etc.).[23,56,57] In our system, the number of ALD cycles was optimized to maximize tunnelling efficiency while avoiding platinizing the substrate (i.e., the PEC effect is lost, and the device simply behaves as a Pt WE).

3.4.2. SEM Analysis of Pt Nanoparticles Deposited on Si(111)|CH_3|Al_2O_3-10. SEM images were obtained (Figure 12) following ALD of platinum from [(MeCp)Pt(Me)$_3$] on Si(111)|Al_2O_3-10 at 240 °C. At 50 cycles (the minimum to see any Pt-enhanced electron transfer in the PEC experiment), the SEM images reveal the formation of nanoparticles (NPs) on the surface. As shown in Figure 12a, the Pt NPs (white dots) are sparsely deposited on the Si|CH_3|Al_2O_3-10 substrate. Following 100 and 150 cycles (Figures 12b,c), both the number and size of the Pt NPs is increased. The grain-size of the Pt NPs on the 100-cycle sample exhibits a diameter of 8.2 ± 1.5 nm, while the substrate treated with 150-cycle growth shows slightly increased diameter metrics of 12.3 ± 2.25 nm. At

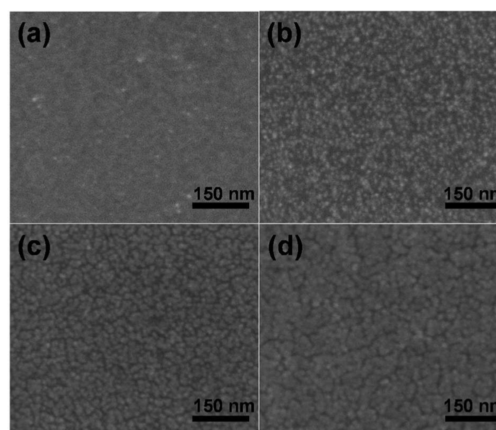

Figure 12. SEM images for Si(111)|CH_3|Al_2O_3-10 depending on Pt ALD cycles: (a) 50, (b) 100, (c) 150, and (d) 200 ALD cycles.

200 cycles of Pt ALD (Figure 12d), the nanoparticles again become larger (16.5 ± 3.0 nm) and more densely populated, wherein the nanoparticles are visibly and consistently in contact with one another. However, Pt deposition of 200 (or more) cycles invariably led to complete platinization of the substrate, entailing loss of the observed PEC effect of Si. Atomic force microscopy (AFM) was also used to quantify the size of the Pt nanoparticles. From the comparison of the AFM and SEM quantification of nanoparticle size (Figure S6, Supporting Information), we concluded SEM provides an equally accurate measurement of particle size in this regime of Pt NPs.

These results are broadly consistent (although with different conditions) to previous reports of Pt deposition by ALD using this precursor. For example, George and co-workers also prepared Pt NPs by the ALD method, utilizing an ALD-prepared Al_2O_3 substrate. Their method also employed [(MeCp)Pt(Me)$_3$], but at higher temperature (300 °C) and using O_2 plasma as the counter-reactant.[55] This plasma-O_2 method achieved short lag phase (only 40 cycles), after which a constant growth rate of 0.5 Å/cycle was observed. One hundred cycles of growth afforded smaller Pt particles (4.3 nm grain size) than those observed in the present work, suggesting that plasma growth may afford advantages in both growth rate and particle size. In the present case, due to instrumental limitations and the sensitivity of the Si(111)|CH_3 substrate to plasma O_2, this deposition method was not attempted. In a more relevant report, Roxhed and co-workers used an analogous set of deposition conditions (Al_2O_3 substrate, O_2 counter-reactant, 250 °C) and reported a lag phase of 125 cycles for Pt growth.[23] Following the lag phase, the observed growth rate was reported as 0.8 Å/cycle, a value similar to the estimated nanoparticle growth rate (Δ_{diam}) of 0.785 Å/cycle in this work.

3.4.3. Enhanced Electron Transfer through Al_2O_3 on n-Si(111)|CH_3|Al_2O_3|Pt-100. To determine the effect of the deposited Pt NPs on electron transfer, a thickness dependence study was again performed (in this case with Pt), analogous to those performed on the Pt-free Si|CH_3|Al_2O_3 samples (Part 3.1.2). Figure 13 shows the observed J_{ox} current of n-Si(111)|CH_3|Al_2O_3|Pt-100 at varying Al_2O_3 thicknesses. The raw data for the Pt-deposited cyclic voltammograms are presented in Supporting Information (Figure S7a, without Pt, and b, with Pt). The n-Si(111)|CH_3|Al_2O_3|Pt-100 sample shows that the Al_2O_3 (up to 34 Å) exhibit minimally resistive behavior, and even the ~50 Å sample retains ~70% of J_{ox}. This compares

DOI: 10.1021/acsami.5b00376
ACS Appl. Mater. Interfaces 2015, 7, 8572−8584

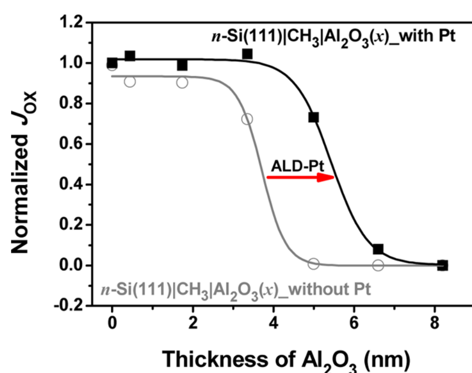

Figure 13. Plot of maximum oxidation current for n-Si(111)|CH_3 with 100-cycle ALD Pt samples depending on Al_2O_3 thickness in 2 mM ferrocene, 0.3 M $LiClO_4$ acetonitrile. The current density of samples without Pt was reproduced from Figure 3.

favorably to the threshold for conformal, 2D growth of Al_2O_3 as determined by the XPS and EIS experiments. However, the ~65 Å film thickness diminishes the observed photocurrent, and the ~80 Å film is nearly completely resistive. This summary plot of the observed current density for each thickness indicates a marked shift in resistivity as compared to the same set of measurements on n-Si(111)|CH_3, wherein the ~50 Å thickness of Al_2O_3 exhibits nearly complete loss of the photocurrent. Overall, these results suggest that a protective, conformal, and pinhole-free ultrathin film of Al_2O_3 decorated with Pt NPs can extend the stability and anodic operation window of Si photoanodes without any compromise in device performance (e.g., J_{max}).

Indeed, several recent precedents for similar effects in MIM devices warrant brief discussion. For example, the "rescue" effect of a single Pt nanoparticle was observed recently on a platinum ultramicroelectrode (UME), and arguments regarding density of states have been put forth to explain this phenomenon.[20] In related work, Fermín and co-workers have investigated a series of "sandwich" electrodes composed of a gold working electrode, a SAM interface, a polyelectrolyte membrane (PEM, controlled thickness), and Au nanoparticles.[19,58,59] The electrochemical response (CV) to a soluble redox marker (aqueous ferro/ferricyanide) was attenuated by the combination of the C10 SAM and the PEM layer. However, deposition of Au nanoparticles on the resulting Au|SAM|PEM|Au-NP electrode rescued the original CV response to that found on the bare Au electrode. Additionally, this behavior was observed with or without an intervening layer of SiO_2 nanoparticles, thus excluding the possibility that the Au nanoparticles protrude through the soft SAM/PEM barrier.

In 2010, Chazalviel et al. provided a theoretical framework to understand such apparently unimpeded electron transfer at metal|insulator|metal junctions between ~5−30 Å.[22] Briefly, these researchers considered a gas-kinetic-theory approach that explains metal → metal electron transfer that is dependent on the overlapping densities of states between the two metal phases. With this work clearly in mind, a recent report by Gooding and co-workers[21] has specifically and systematically tested this hypothesis by generating glassy carbon substrates with varying thicknesses of an organic insulator, followed by deposition of gold nanoparticles. These researchers found a thickness independent region from 0−20 Å of insulator, followed by a thickness-dependent region at >20 Å. These results appear quite similar to the present case of Al_2O_3 thickness dependence using Pt NPs for enhanced ET, thus implying that the metal → metal electron transfer via density of states holds for semiconductor devices, as well, as predicted in the Chazalviel report.

4. CONCLUSION

We summarize our findings as follows:

(1) Ultrathin films of ALD-deposited Al_2O_3 (1−10 Å) on methylated Si(111)|CH_3 electrodes are deposited first in a 3D island growth mode that is characterized by high capacitance attributed to a large extent of Al and O vacancies in the nascent film.

(2) At greater thicknesses (10−34 Å), the Al_2O_3 film is deposited in a conformal, pinhole-free 2D-growth mode that is characterized by a rapidly diminishing capacitance, which is attributed to a smaller number of Al and O defect sites in the "bulk" Al_2O_3 film. Electrochemical stability measurements show that the protective Al_2O_3 film provides an enhanced anodic operation window and aqueous stability.

(3) An organic monolayer on Si(111) surfaces [such as Si(111)|CH_3 used here] is required before ALD deposition of the Al_2O_3 thin films to retain photoresponse at solid|liquid junctions in a PEC cell. The ALD process on HF-etched Si(111)−H surfaces results in no PEC response and poor electronic properties.

(4) In scan-rate dependence studies, experimental and simulated data suggest that a rational choice of redox couple and solvent/electrolyte based on diffusion constant can facilitate interrogation of barrier layers (in this case Al_2O_3) of different thicknesses with varying precision.

(5) Although the thickness of Al_2O_3 required to generate a conformal, pinhole-free film imparts significant resistive behavior in PEC experiments, the J_{max} can be effectively rescued by the deposition of Pt nanoparticles by a low-temperature, O_2-based ALD process. This synergistic combination of Al_2O_3 and Pt thus enhances the scope of operation and stability of Si photoanodes, which is especially unique on the surface defect-prone Si(111) facet.

(6) Throughout the multistep assembly process, the Si(111) substrates experience increased temperatures during ALD of Al_2O_3 (150 °C) and Pt (240 °C), as well as exposure to ambient atmosphere and light. Nonetheless, the n-Si(111)|CH_3|Al_2O_3-50 Å|Pt-100 device retains excellent electronic properties (PEC, SRV, EIS), low surface oxide content (XPS), and a low defect density versus the "bare" n-Si(111)|CH_3 sample.

■ ASSOCIATED CONTENT

Ⓢ Supporting Information

Schematic diagram of PEC cell; reflectance spectra; extended CV simulations; assigned post-PEC XPS spectra; and cyclic voltammograms depending on the number of Al_2O_3 ALD cycles. This material is available free of charge via the Internet at http://pubs.acs.org.

■ AUTHOR INFORMATION

Corresponding Author

*E-mail: mrose@cm.utexas.edu.

Notes

The authors declare no competing financial interest.

DOI: 10.1021/acsami.5b00376
ACS Appl. Mater. Interfaces 2015, 7, 8572−8584

■ ACKNOWLEDGMENTS

This research was supported by the U.S. Office of Naval Research (N00014-13-1-0530), the Robert A. Welch Foundation (F-1822), the American Chemical Society PRF program (53542-DN13), and the UT Austin College of Natural Sciences. K.L.K. gratefully acknowledges support from the Semiconductor Research Corporation undergraduate research initiative. Funding for the Kratos Axis Ultra XPS was provided by a grant from the National Science Foundation (MRI-0618242).

■ REFERENCES

(1) Du, P.; Eisenberg, R. Catalysts Made of Earth-Abundant Elements (Co, Ni, Fe) for Water Splitting: Recent Progress and Future Challenges. *Energy Environ. Sci.* **2012**, *5*, 6012−6021.

(2) Mayer, M. T.; Lin, Y.; Yuan, G.; Wang, D. Forming Heterojunctions at the Nanoscale for Improved Photoelectrochemical Water Splitting by Semiconductor Materials: Case Studies on Hematite. *Acc. Chem. Res.* **2013**, *46*, 1558−1566.

(3) Newman, J.; Hoertz, P. G.; Bonino, C. A.; Trainham, J. A. Review: An Economic Perspective on Liquid Solar Fuels. *J. Electrochem. Soc.* **2012**, *159*, A1722−A1729.

(4) Kenney, M. J.; Gong, M.; Li, Y.; Wu, J. Z.; Feng, J.; Lanza, M.; Dai, H. High-Performance Silicon Photoanodes Passivated with Ultrathin Nickel Films for Water Oxidation. *Science* **2013**, *342*, 836−840.

(5) Dominey, R. N.; Lewis, N. S.; Bruce, J. A.; Bookbinder, D. C.; Wrighton, M. S. Improvement of Photoelectrochemical Hydrogen Generation by Surface Modification of p-Type Silicon Semiconductor Photocathodes. *J. Am. Chem. Soc.* **1982**, *104*, 467−482.

(6) Bansal, A.; Li, X.; Lauermann, I.; Lewis, N. S.; Yi, S. I.; Weinberg, W. H. Alkylation of Si Surfaces Using a Two-Step Halogenation/Grignard Route. *J. Am. Chem. Soc.* **1996**, *118*, 7225−7226.

(7) Bansal, A.; Lewis, N. S. Stabilization of Si Photoanodes in Aqueous Electrolytes through Surface Alkylation. *J. Phys. Chem. B* **1998**, *102*, 4058−4060.

(8) Webb, L. J.; Lewis, N. S. Comparison of the Electrical Properties and Chemical Stability of Crystalline Silicon(111) Surfaces Alkylated Using Grignard Reagents or Olefins with Lewis Acid Catalysts. *J. Phys. Chem. B* **2003**, *107*, 5404−5412.

(9) Nemanick, E. J.; Hurley, P. T.; Brunschwig, B. S.; Lewis, N. S. Chemical and Electrical Passivation of Silicon (111) Surfaces through Functionalization with Sterically Hindered Alkyl Groups. *J. Phys. Chem. B* **2006**, *110*, 14800−14808.

(10) Cicero, R. L.; Linford, M. R.; Chidsey, C. E. D. Photoreactivity of Unsaturated Compounds with Hydrogen-Terminated Silicon(111). *Langmuir* **2000**, *16*, 5688−5695.

(11) Liang, W.; Weber, K. J.; Suh, D.; Phang, S. P.; Yu, J.; McAuley, A. K.; Legg, B. R. Surface Passivation of Boron-Diffused p-Type Silicon Surfaces with (100) and (111) Orientations by ALD Al_2O_3 Layers. *IEEE J. Photovolt.* **2013**, *3*, 678−683.

(12) Dingemans, G.; Kessels, W. M. M. Status and Prospects of Al_2O_3-Based Surface Passivation Schemes for Silicon Solar Cells. *J. Vac. Sci. Technol., A* **2012**, *30*, 040802.

(13) Kalanyan, B.; Parsons, G. Atomic Layer Deposited Oxides for Passivation of Silicon Photoelectrodes for Solar Photoelectrochemical Cells. *ECS Trans.* **2011**, *41*, 285−292.

(14) Terlinden, N. M.; Dingemans, G.; van de Sanden, M. C. M.; Kessels, W. M. M. Role of Field-Effect on *c*-Si Surface Passivation by Ultrathin (2−20 nm) Atomic Layer Deposited Al_2O_3. *Appl. Phys. Lett.* **2010**, *96*, 112101.

(15) Dingemans, G.; Terlinden, N. M.; Pierreux, D.; Profijt, H. B.; van de Sanden, M. C. M.; Kessels, W. M. M. Influence of the Oxidant on the Chemical and Field-Effect Passivation of Si by ALD Al_2O_3. *Electrochem. Solid-State Lett.* **2011**, *14*, H1−H4.

(16) Gao, K. Y.; Speck, F.; Emtsev, K.; Seyller, T.; Ley, L. Thermal Stability of Surface and Interface Structure of Atomic Layer Deposited Al_2O_3 on H-Terminated Silicon. *J. Appl. Phys.* **2007**, *102*, 094503.

(17) Johnson, R. S.; Lucovsky, G.; Baumvol, I. Physical and Electrical Properties of Noncrystalline Al_2O_3 Prepared by Remote Plasma Enhanced Chemical Vapor Deposition. *J. Vac. Sci. Technol., A* **2001**, *19*, 1353−1360.

(18) Groner, M. D.; Elam, J. W.; Fabreguette, F. H.; George, S. M. Electrical Characterization of Thin Al_2O_3 Films Grown by Atomic Layer Deposition on Silicon and Various Metal Substrates. *Thin Solid Films* **2002**, *413*, 186−197.

(19) Zhao, J.; Wasem, M.; Bradbury, C. R.; Fermín, D. J. Charge Transfer across Self-Assembled Nanoscale Metal−Insulator−Metal Heterostructures. *J. Phys. Chem. C* **2008**, *112*, 7284−7289.

(20) Kim, J.; Kim, B.-K.; Cho, S. K.; Bard, A. J. Tunneling Ultramicroelectrode: Nanoelectrodes and Nanoparticle Collisions. *J. Am. Chem. Soc.* **2014**, *136*, 8173−8176.

(21) Barfidokht, A.; Ciampi, S.; Luais, E.; Darwish, N.; Gooding, J. J. Distance-Dependent Electron Transfer at Passivated Electrodes Decorated by Gold Nanoparticles. *Anal. Chem.* **2012**, *85*, 1073−1080.

(22) Chazalviel, J.-N.; Allongue, P. On the Origin of the Efficient Nanoparticle Mediated Electron Transfer across a Self-Assembled Monolayer. *J. Am. Chem. Soc.* **2010**, *133*, 762−764.

(23) Pardon, G.; Gatty, H. K.; Stemme, G.; van der Wijngaart, W.; Roxhed, N. Pt−Al_2O_3 Dual Layer Atomic Layer Deposition Coating in High Aspect Ratio Nanopores. *Nanotechnology* **2013**, *24*, 015602.

(24) Hämäläinen, J.; Puukilainen, E.; Sajavaara, T.; Ritala, M.; Leskelä, M. Low Temperature Atomic Layer Deposition of Noble Metals Using Ozone and Molecular Hydrogen as Reactants. *Thin Solid Films* **2013**, *531*, 243−250.

(25) Brundle, C. R.; Conti, G.; Mack, P. XPS and Angle Resolved XPS, in the Semiconductor Industry: Characterization and Metrology Control of Ultra-Thin Films. *J. Electron Spectrosc. Relat. Phenom.* **2010**, *178−179*, 433−448.

(26) Renault, O.; Gosset, L. G.; Rouchon, D.; Ermolieff, A. Angle-Resolved X-Ray Photoelectron Spectroscopy of Ultrathin Al_2O_3 Films Grown by Atomic Layer Deposition. *J. Vac. Sci. Technol., A* **2002**, *20*, 1867−1876.

(27) Lu, Z. H.; McCaffrey, J. P.; Brar, B.; Wilk, G. D.; Wallace, R. M.; Feldman, L. C.; Tay, S. P. SiO_2 Film Thickness Metrology by X-Ray Photoelectron Spectroscopy. *Appl. Phys. Lett.* **1997**, *71*, 2764−2766.

(28) Lattimer, J. R. C.; Brunschwig, B. S.; Lewis, N. S.; Gray, H. B. Redox Properties of Mixed Methyl/Vinylferrocenyl Monolayers on Si(111) Surfaces. *J. Phys. Chem. C* **2013**, *117*, 27012−27022.

(29) Amatore, C.; Savéant, J. M.; Tessier, D. Charge Transfer at Partially Blocked Surfaces: A Model for the Case of Microscopic Active and Inactive Sites. *J. Electroanal. Chem.* **1983**, *147*, 39−51.

(30) Nicholson, R. S.; Shain, I. Theory of Stationary Electrode Polarography. Single Scan and Cyclic Methods Applied to Reversible, Irreversible, and Kinetic Systems. *Anal. Chem.* **1964**, *36*, 706−723.

(31) Reinmuth, W. H. Nernst-Controlled Currents in Hanging-Drop Polarography. *J. Am. Chem. Soc.* **1957**, *79*, 6358−6360.

(32) Elam, J. W.; Zinovev, A. V. V; Pellin, M. J.; Comstock, D. J.; Hersam, M. C. Nucleation and Growth of Noble Metals on Oxide Surfaces Using Atomic Layer Deposition. *ECS Trans.* **2007**, *3*, 271−278.

(33) Puurunen, R. L.; Vandervorst, W.; Besling, W. F. A.; Richard, O.; Bender, H.; Conard, T.; Zhao, C.; Delabie, A.; Caymax, M.; De Gendt, S.; Heyns, M.; Viitanen, M. M.; de Ridder, M.; Brongersma, H. H.; Tamminga, Y.; Dao, T.; de Win, T.; Verheijen, M.; Kaiser, M.; Tuominen, M. Island Growth in the Atomic Layer Deposition of Zirconium Oxide and Aluminum Oxide on Hydrogen-Terminated Silicon: Growth Mode Modeling and Transmission Electron Microscopy. *J. Appl. Phys.* **2004**, *96*, 4878−4889.

(34) Tripathi, J. K.; Garbrecht, M.; Kaplan, W. D.; Markovich, G.; Goldfarb, I. The Effect of Fe-Coverage on the Structure, Morphology and Magnetic Properties of α-$FeSi_2$ Nanoislands. *Nanotechnology* **2012**, *23*, 495603.

DOI: 10.1021/acsami.5b00376
ACS Appl. Mater. Interfaces 2015, 7, 8572−8584

(35) Cai, W.; Lin, Z.; Strother, T.; Smith, L. M.; Hamers, R. J. Chemical Modification and Patterning of Iodine-Terminated Silicon Surfaces Using Visible Light. *J. Phys. Chem. B* **2002**, *106*, 2656−2664.
(36) Yu, H.; Webb, L. J.; Ries, R. S.; Solares, S. D.; Goddard, W. A.; Heath, J. R.; Lewis, N. S. Low-Temperature STM Images of Methyl-Terminated Si(111) Surfaces. *J. Phys. Chem. B* **2004**, *109*, 671−674.
(37) Some, S.; Ho, S.-M.; Dua, P.; Hwang, E.; Shin, Y. H.; Yoo, H.; Kang, J.-S.; Lee, D.-K.; Lee, H. Dual Functions of Highly Potent Graphene Derivative−Poly-L-Lysine Composites to Inhibit Bacteria and Support Human Cells. *ACS Nano* **2012**, *6*, 7151−7161.
(38) Yumitori, S. Correlation of C1s Chemical State Intensities with the O1s Intensity in the XPS Analysis of Anodically Oxidized Glass-Like Carbon Samples. *J. Mater. Sci.* **2000**, *35*, 139−146.
(39) Puniredd, S. R.; Assad, O.; Haick, H. Highly Stable Organic Modification of Si(111) Surfaces: Towards Reacting Si with Further Functionalities while Preserving the Desirable Chemical Properties of Full Si−C Atop Site Terminations. *J. Am. Chem. Soc.* **2008**, *130*, 9184−9185.
(40) Díaz, B.; Härkönen, E.; Światowska, J.; Maurice, V.; Seyeux, A.; Marcus, P.; Ritala, M. Low-Temperature Atomic Layer Deposition of Al_2O_3 Thin Coatings for Corrosion Protection of Steel: Surface and Electrochemical Analysis. *Corros. Sci.* **2011**, *53*, 2168−2175.
(41) Kloprogge, J. T.; Duong, L. V.; Wood, B. J.; Frost, R. L. XPS Study of the Major Minerals in Bauxite: Gibbsite, Bayerite and (Pseudo-)Boehmite. *J. Colloid Interface Sci.* **2006**, *296*, 572−576.
(42) Kenneth, D. L.; Arthur, B. E.; Jeffrey, M. B.; Mark, S. W. N-Type Si-Based Photoelectrochemical Cell: New Liquid Junction Photocell Using a Nonaqueous Ferricenium/Ferrocene Electrolyte. *Proc. Natl. Acad. Sci. U.S.A.* **1977**, *74*, 4116−4120.
(43) Satpati, A. K.; Arroyo-Currás, N.; Ji, L.; Yu, E. T.; Bard, A. J. Electrochemical Monitoring of TiO_2 Atomic Layer Deposition by Chronoamperometry and Scanning Electrochemical Microscopy. *Chem. Mater.* **2013**, *25*, 4165−4172.
(44) van de Lagemaat, J.; Park, N. G.; Frank, A. J. Influence of Electrical Potential Distribution, Charge Transport, and Recombination on the Photopotential and Photocurrent Conversion Efficiency of Dye-Sensitized Nanocrystalline TiO_2 Solar Cells: A Study by Electrical Impedance and Optical Modulation Techniques. *J. Phys. Chem. B* **2000**, *104*, 2044−2052.
(45) Gao, X.; Guan, D.; Huo, J.; Chen, J.; Yuan, C. Free Standing TiO_2 Nanotube Array Electrodes with an Ultra-Thin Al_2O_3 Barrier Layer and $TiCl_4$ Surface Modification for Highly Efficient Dye Sensitized Solar Cells. *Nanoscale* **2013**, *5*, 10438−10446.
(46) Liu, D.; Clark, S. J.; Robertson, J. Oxygen Vacancy Levels and Electron Transport in Al_2O_3. *Appl. Phys. Lett.* **2010**, *96*, 032905.
(47) Zhang, Y.; Seghete, D.; Abdulagatov, A.; Gibbs, Z.; Cavanagh, A.; Yang, R.; George, S.; Lee, Y.-C. Investigation of the Defect Density in Ultra-Thin Al_2O_3 Films Grown Using Atomic Layer Deposition. *Surf. Coat. Technol.* **2011**, *205*, 3334−3339.
(48) Clegg, A. D.; Rees, N. V.; Klymenko, O. V.; Coles, B. A.; Compton, R. G. Marcus Theory of Outer-Sphere Heterogeneous Electron Transfer Reactions: High Precision Steady-State Measurements of the Standard Electrochemical Rate Constant for Ferrocene Derivatives in Alkyl Cyanide Solvents. *J. Electroanal. Chem.* **2005**, *580*, 78−86.
(49) Cannes, C.; Kanoufi, F.; Bard, A. J. Cyclic Voltammetry and Scanning Electrochemical Microscopy of Ferrocenemethanol at Monolayer and Bilayer-Modified Gold Electrodes. *J. Electroanal. Chem.* **2003**, *547*, 83−91.
(50) Zanello, P. *Inorganic Electrochemistry: Theory, Practice and Applications*; Royal Society of Chemistry: Cambridge, U.K., 2003; pp 62−63.
(51) Geiger, W. E. Chemical Reversibility. In *Inorganic Reactions and Methods, Electron-Transfer and Electrochemical Reactions; Photochemical and Other Energized Reactions*; Zuckerman, J. J., Hagen, A. P., Eds.; Wiley: New York, 2009; Vol. *15*, p 90.
(52) Miao, W.; Ding, Z.; Bard, A. J. Solution Viscosity Effects on the Heterogeneous Electron Transfer Kinetics of Ferrocenemethanol in Dimethyl Sulfoxide−Water Mixtures. *J. Phys. Chem. B* **2002**, *106*, 1392−1398.
(53) Himpsel, F. J.; McFeely, F. R.; Taleb-Ibrahimi, A.; Yarmoff, J. A.; Hollinger, G. Microscopic Structure of the SiO_2/Si Interface. *Phys. Rev. B: Condens. Matter Mater. Phys.* **1988**, *38*, 6084−6096.
(54) Hattori, T. Surface, Interface, and Valence Band Structures of Ultra-Thin Silicon Oxides. *Appl. Surf. Sci.* **1998**, *130−132*, 156−164.
(55) Baker, L.; Cavanagh, A. S.; Seghete, D.; George, S. M.; Mackus, A. J. M.; Kessels, W. M. M.; Liu, Z. Y.; Wagner, F. T. Nucleation and Growth of Pt Atomic Layer Deposition on Al_2O_3 Substrates Using (Methylcyclopentadienyl)-Trimethyl Platinum and O_2 Plasma. *J. Appl. Phys.* **2011**, *109*, 084333.
(56) Sun, S.; Zhang, G.; Gauquelin, N.; Chen, N.; Zhou, J.; Yang, S.; Chen, W.; Meng, X.; Geng, D.; Banis, M. N.; Li, R.; Ye, S.; Knights, S.; Botton, G. A.; Sham, T.-K.; Sun, X. Single-Atom Catalysis Using Pt/Graphene Achieved through Atomic Layer Deposition. *Sci. Rep.* **2013**, *3*, 1775.
(57) Ding, S.-J.; Chen, H.-B.; Cui, X.-M.; Chen, S.; Sun, Q.-Q.; Zhou, P.; Lu, H.-L.; Zhang, D. W.; Shen, C. Atomic Layer Deposition of High-Density Pt Nanodots on Al_2O_3 Film Using $(MeCp)Pt(Me)_3$ and O_2 Precursors for Nonvolatile Memory Applications. *Nanoscale Res. Lett.* **2013**, *8*, 80.
(58) Zhao, J.; Bradbury, C. R.; Fermín, D. J. Long-Range Electronic Communication between Metal Nanoparticles and Electrode Surfaces Separated by Polyelectrolyte Multilayer Films. *J. Phys. Chem. C* **2008**, *112*, 6832−6841.
(59) Bradbury, C. R.; Zhao, J.; Fermín, D. J. Distance-Independent Charge-Transfer Resistance at Gold Electrodes Modified by Thiol Monolayers and Metal Nanoparticles. *J. Phys. Chem. C* **2008**, *112*, 10153−10160.

DOI: 10.1021/acsami.5b00376
ACS Appl. Mater. Interfaces 2015, 7, 8572−8584